Accuracy of unperturbed motion of particles in a gyrokinetic semi-Lagrangian code

G. Latu, V. Grandgirard, J. Abiteboul, M. Bergot, N. Crouseilles, X. Garbet, P. Ghendrih, M. Mehrenberger, Y. Sarazin, H. Sellama, E. Sonnendrücker, D. Zarzoso

RESEARCH REPORT
N° 8054
September 2012
Project-Teams CALVI & IPSO

ISSN 0249-6399 ISRN INRIA/RR--8054--FR+ENG

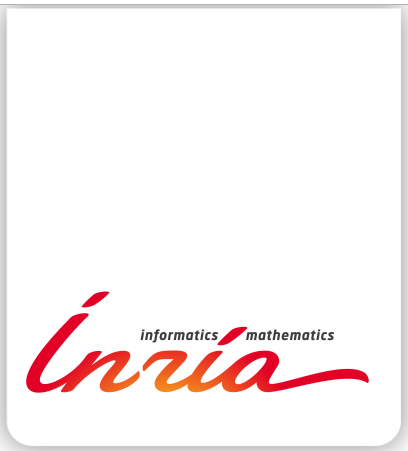

Accuracy of unperturbed motion of particles in a gyrokinetic semi-Lagrangian code

G. Latu*, V. Grandgirard*, J. Abiteboul*, M. Bergot†, N. Crouseilles‡, X. Garbet*, P. Ghendrih*, M. Mehrenberger†, Y. Sarazin*, H. Sellama†, E. Sonnendrücker†, D. Zarzoso*

Project-Teams CALVI & IPSO

Research Report n° 8054 — September 2012 — 14 pages

Abstract: Inaccurate description of the equilibrium can yield to spurious effects in gyrokinetic turbulence simulations. Also, the Vlasov solver and time integration schemes impact the conservation of physical quantities, especially in long-term simulations. Equilibrium and Vlasov solver have to be tuned in order to preserve constant states (equilibrium) and to provide good conservation property along time (mass to begin with). Several illustrative simple test cases are given to show typical spurious effects that one can observes for poor settings. We explain why Forward Semi-Lagrangian scheme bring us some benefits. Some toroidal and cylindrical GYSELA runs are shown that use FSL.

Key-words: gyrokinetic, conservation laws, FSL

* CEA Cadarache, IRFM bat. 513, 13108 Saint-Paul-les-Durance
† University of Strasbourg, 7 rue Descartes, 67000 Strasbourg & INRIA CALVI
‡ INRIA IPSO & IRMAR, 263 av Général Leclerc, 35042 Rennes

RESEARCH CENTRE
NANCY – GRAND EST

615 rue du Jardin Botanique
CS20101
54603 Villers-lès-Nancy Cedex

Précision du mouvement de particules non perturbées dans un code gyrocinétique

Résumé : Une description imparfaite de l'équilibre peut conduire à des artéfacts numériques dans des simulations turbulentes gyrocinétiques. Aussi, le solveur de Vlasov and le schéma d'intégration en temps ont un impact fort sur la conservation de quantités physiques, notamment lorsque les simulations sont en temps long. L'équilibre et le solveur Vlasov doivent être finement choisis et paramétrés pour conserver les états constants (équilibre) et pour autoriser de bonnes propriétés de conservation en temps (en commençant par la conservation de la masse). Plusieurs cas tests illustratifs sont donnés pour montrer les problèmes numériques typiques que l'on peut observer si les choix pris ne sont pas adéquats. Nous expliquons pourquoi le schéma FSL (Forward Semi-Lagrangian) apporte une réponse à certains problèmes. Des simulations en configuration cylindrique et torique de GYSELA sont présentées qui utilisent FSL.

Mots-clés : gyrocinétique, lois de conservation, FSL

1 Introduction

Inaccurate description of the gyrokinetic equilibrium can yield unphysical excitation of zonal flow oscillations[ABH+06]. Moreover, as stated in [IIK+08], it is important to define the initial condition using a relevant gyrokinetic equilibrium, especially in collisionless full-f simulations. In the following, accuracy aspects are investigated for both the gyrokinetic equilibrium and the Vlasov solver used in the GYSELA code. If proper care is not taken for Vlasov solver and gyrokinetic initial equilibrium, one can observe that some conservation properties are not satisfied, for example mass conservation.

The gyrokinetic framework of the study is explained in the next section. Then, quite experimental investigations are shown to understand numerics associated with equilibrium and mass conservation. Forward Semi-Lagrangian (FSL) scheme is presented briefly. The splitting in a linear and a non-linear part of the Vlasov equation is explained. Results of numerical simulation for 4D cylindrical test cases and toroidal test cases are presented in the last section. Forward Semi-Lagrangian scheme helps a lot to preserve good accuracy on mass and total energy.

2 Description of the context

2.1 Gyrokinetic Vlasov equation

The time evolution of the gyro-center coordinates $(\vec{x}, v_\parallel, \mu)$ of species s is given by the collisionless electrostatic gyrokinetic equations:

$$\frac{\mathrm{d}x^i}{\mathrm{dt}} = v_\parallel \vec{b}^*_s \cdot \vec{\nabla} x^i + \vec{v}_{Es_{GC}} \cdot \vec{\nabla} x^i + \vec{v}_{Ds} \cdot \vec{\nabla} x^i \tag{1}$$

$$m_s \frac{\mathrm{d}v_\parallel}{\mathrm{dt}} = -\mu \vec{b}^*_s \cdot \vec{\nabla} B - e_s \vec{b}^*_s \cdot \vec{\nabla} \bar{\phi} + \frac{m_s v_\parallel}{B} \vec{v}_{Es_{GC}} \cdot \vec{\nabla} B \tag{2}$$

where x^i corresponds to the i-th covariant coordinate of $\vec{x}$, B is the magnetic field and $B^*_{\parallel s}$ and $\vec{b}^*_s$ are defined as:

$$B^*_{\parallel s} = B + \frac{m_s v_\parallel}{e_s B} \mu_0 \vec{b} \cdot \vec{J} \tag{3}$$

$$\vec{b}^*_s = \frac{\vec{B}}{B^*_{\parallel s}} + \frac{m_s v_\parallel}{e_s B^*_{\parallel s}} \frac{\mu_0 \vec{J}}{B} \tag{4}$$

The advection terms are:

$$\vec{b}^*_s \cdot \vec{\nabla} x^i = b^{*i}_s = \frac{\vec{B} \cdot \vec{\nabla} x^i}{B^*_{\parallel s}} + \frac{m_s v_\parallel}{e_s B^*_{\parallel s}} \frac{\mu_0 \vec{J} \cdot \vec{\nabla} x^i}{B} \tag{5}$$

$$\vec{v}_{Ds} \cdot \vec{\nabla} x^i = v^i_{Ds} = \left(\frac{m_s v_\parallel^2 + \mu B}{e_s B^*_{\parallel s} B} \right) [B, x^i] \tag{6}$$

$$\vec{v}_{Es_{GC}} \cdot \vec{\nabla} x^i = v^i_{Es_{GC}} = \frac{1}{B^*_{\parallel s}} [\bar{\phi}, x^i] \tag{7}$$

$$\vec{v}_{Es_{GC}} \cdot \vec{\nabla} B = -\frac{1}{B^*_{\parallel s}} [B, \bar{\phi}] \tag{8}$$

the Poisson bracket is defined by $[F,G] = \vec{b} \cdot (\vec{\nabla} F \times \vec{\nabla} G)$. The velocity parallel to the magnetic field is $v_\parallel$. The magnetic moment $\mu = m_s v_\perp^2/(2B)$ is an adiabatic invariant with $v_\perp$ the velocity in the plane orthogonal to the magnetic field. Vacuum permittivity is denoted μ_0. The term $v_{E_{GC}}$ represents the electric $E \times B$ drift velocity of the guiding-centers and v_D the curvature drift velocity. The Jacobian in phase space is $J_s(r,\theta) B^*_{||s}(r,\theta,v_\parallel)$.

Some references concerning the framework we use to solve this equation can be found in [GBB+06, GSG+08, BCG+11, SGA+11, AGG+11].

2.2 Quasineutrality equation

The quasineutrality equation and parallel Ampère's law close the self-consistent gyrokinetic Vlasov-Maxwell system. However, in an electrostatic code, the field solver reduces to the numerical solving of a Poisson-like equation [Hah88]. In tokamak configurations, the plasma

quasineutrality (denoted QN) approximation is currently assumed [GBB+06]. Electron inertia is ignored, which means that an adiabatic response of electrons is supposed. We define the operator $\nabla_\perp = (\partial_r, \frac{1}{r}\partial_\theta)$. We note n_0 the equilibrium density, B_0 the magnetic field at the magnetic axis and $T_e(r)$ the electronic temperature. We have also $B(r,\theta)$ the magnetic field, J_0 the Bessel function of first order and $k_\perp$ the transverse component of the wave vector. Hence, the QN equation can be written in dimensionless variables

$$-\frac{1}{n_0(r)}\nabla_\perp \cdot \left[\frac{n_0(r)}{B_0}\nabla_\perp \Phi(r,\theta,\varphi)\right] + \frac{1}{T_e(r)}\left[\Phi(r,\theta,\varphi) - \langle\Phi\rangle_{FS}(r)\right] = \tilde{\rho}(r,\theta,\varphi) \tag{9}$$

where $\tilde{\rho}$ is defined by

$$\tilde{\rho}(r,\theta,\varphi) = \frac{2\pi}{n_0(r)}\int B^*_{\|s} d\mu \int dv_\| J_0(k_\perp\sqrt{2\mu})(\bar{f} - \bar{f}_{eq})(r,\theta,\varphi,v_\|,\mu). \tag{10}$$

with $\bar{f}_{eq}$ representing local ion Maxwellian equilibrium, and $\langle . \rangle_{FS}(r)$ the average on the flux surface labelled by r.

3 Unperturbed motion of particles

3.1 Simplification of the equations

Let suppose that a collisionless equilibrium distribution function f_{eq} is taken for the initial distribution function: $f_{t=0}(r,\theta,\varphi,v_\|)$. By definition, if the Vlasov and Quasi-neutrality equations are accurately solved, the distribution function f_t should remain constant over time, *i.e.* equal to f_{eq}. Also, the electric potential $\Phi(r,\theta,\varphi)$ should remain equal to zero because the right hand side of the Quasi-neutrality equation, the integral of $f - f_{eq}$, is zero.
Then, one quantitative measure of Vlasov solver accuracy is its capability to preserve an equilibrium distribution function over time, assuming $\Phi = 0$. In order to get a simple tool to evaluate the Vlasov solver, one can also restrict to the case $\mu = 0$. It is worthwhile rewriting gyrokinetic equations in this reduced setting:

$$\frac{\mathrm{d}x^i}{\mathrm{dt}} = v_\| \vec{b}^*_s \cdot \vec{\nabla} x^i + \vec{v}_{Ds} \cdot \vec{\nabla} x^i \tag{11}$$

$$m_s \frac{\mathrm{d}v_\|}{\mathrm{dt}} = 0 \tag{12}$$

It gives

$$\frac{\mathrm{d}x^i}{\mathrm{dt}} = \frac{\vec{B}\cdot\vec{\nabla}x^i}{B^*_{\|s}} v_\| + \frac{m_s {v_\|}^2}{e_s B^*_{\|s}} \frac{\mu_0 \vec{J}\cdot\vec{\nabla}x^i}{B} + \left(\frac{m_s v_\|^2}{e_s B^*_{\|s} B}\right)[B, x^i] \tag{13}$$

$$\frac{\mathrm{d}v_\|}{\mathrm{dt}} = 0 \tag{14}$$

and finally, assuming that the current J is perpendicular to the poloidal plane,

$$\frac{\mathrm{d}r}{\mathrm{dt}} = \frac{B_r}{B^*_{\|s}} v_\| + \frac{m_s v_\|^2}{e_s B^*_{\|s} B}[B, r] \tag{15}$$

$$\frac{\mathrm{d}\theta}{\mathrm{dt}} = \frac{B_\theta}{B^*_{\|s}} v_\| + \frac{m_s v_\|^2}{e_s B^*_{\|s} B}[B, \theta] \tag{16}$$

$$\frac{\mathrm{d}\varphi}{\mathrm{dt}} = \frac{B_\varphi}{B^*_{\|s}} v_\| + \frac{m_s {v_\|}^2}{e_s B^*_{\|s}} \frac{J_\varphi}{B} + \frac{m_s v_\|^2}{e_s B^*_{\|s} B}[B, \varphi] \tag{17}$$

Particles keep a constant parallel velocity over time. Then the trajectory of one particle in phase space remains in the 3D space dimensions.

3.2 Trajectory of particles

The GYSELA code uses a Semi-Lagrangian scheme combined with a Strang splitting. To guarantee second order accuracy in time, the following sequence [GBB+06] is used: $(\hat{v_\|}/2, \hat{\varphi}/2, \hat{r\theta}, \hat{\varphi}/2, \hat{v_\|}/2)$, where factor $1/2$ denotes a shift over $\Delta t/2$. In this sequence, $\hat{v_\|}$ and $\hat{\varphi}$ shifts correspond to 1D advections along $v_\|$ and φ directions, and $\hat{r\theta}$ represents a 2D advection (displacement in r and θ are strongly coupled). Let us now focus on the discretization of the 2D advection which requires specific attention.

Taylor expansion For a single $\hat{r\theta}$ advection in the semi-Lagrangian approach, a displacement $(\delta r, \delta\theta)$ is computed to find the foot of the characteristics that ends at a grid node (r_i, θ_j). This displacement is computed thanks to a Taylor expansion of the fields acting on particles [GBB+06]. One can derive two fields α and β from Eqs. (15, 16, 17) such as:

$$\begin{pmatrix}\delta r\\ \delta\theta\end{pmatrix}_{(r_i,\theta_j)} = \alpha(r_i,\theta_j)\Delta t + \beta(r_i,\theta_j)\Delta t^2 + O(\Delta t^3)$$

The problem is that, if δr or $\delta\theta$ is larger than grid element sizes denoted Δr and $\Delta\theta$, then this approximation can be really inaccurate.

Precomputed trajectories Another method is described here to find out the foot of the characteristics associated to each grid node. Since the fields acting on particles, Eqs. (11,12), do not depends on time t, one can approximate $(\delta r, \delta\theta)_{(r_i,\theta_j)}$ once for all. We have used Runge-Kutta time integration scheme (RK2) with a small time step to precompute these trajectories. This approach is possible only for the linear terms of Eqs. (11,12), but not for non-linear terms, present in Eqs. (1,2), that depend on E_t and Φ_t. Let us choose a δt, such as $M\,\delta t = \Delta t$ with $M \in \mathbb{N}$ and M large enough. One can build a series r^n and θ^n as follows:

$$\begin{pmatrix}r^{n+\frac{1}{2}}\\ \theta^{n+\frac{1}{2}}\end{pmatrix} = \begin{pmatrix}r^n\\ \theta^n\end{pmatrix} + \frac{\delta t}{2}\,\alpha(r^n,\theta^n)$$

$$\begin{pmatrix}r^{n+1}\\ \theta^{n+1}\end{pmatrix} = \begin{pmatrix}r^n\\ \theta^n\end{pmatrix} + \delta t\;\alpha(r^{n+\frac{1}{2}},\theta^{n+\frac{1}{2}})$$

The initial condition is set to $r^0 = r_i$, $\theta^0 = \theta_j$. After M steps of Runge-Kutta iteration, it gives

$$\begin{pmatrix}\delta r\\ \delta\theta\end{pmatrix}_{(r_i,\theta_j)} = \begin{pmatrix}r^M\\ \theta^M\end{pmatrix}$$

Because these trajectories can be computed only once when the simulation starts, M can be taken quite large (we will assume $M = 64$ in the following). These precomputations will not impact significantly the global simulation time. Other time integration schemes have been tried: RK3, RK4, and also larger values of M, but these modifications does not impact significantly the precision in our test cases.

3.2.1 Forward Semi-Lagrangian scheme

The Forward Semi-Lagrangian scheme [CRS09] (the acronym is FSL) is an alternative to the classical Backward Semi-Lagrangian scheme (BSL). It is based on forward integration of the characteristics. The distribution function is updated on an eulerian grid, and the pseudo-particles located on the mesh nodes follow the characteristics of the equation forward for one time step, and are then deposited on nearest nodes. While the main cost of the BSL method comes from the interpolation step, FSL spends most of computational time in the deposition step. The FSL scheme can be set up such as mass is preserved along time.

We present the approach taken for the 2D advection in (r, θ). In our setting, the algorithm of Forward Semi-Lagrangian is the following (with S the cubic B-spline):

- Step 1: Compute the spline coefficients $w^n_{k,l}$ (f^n is known) such that

$$(J_s B^*_{||s} f^n)_{i,j} = \sum_{k,l} w^n_{k,l} S(x_i - x_k) S(y_j - y_l)$$

- Step 2: Integrate forward in time the characteristics from t^n to t^{n+1}, given as initial data the grid points (x_k, y_l). We obtain the new particle positions $(x^\star_k, y^\star_l)$ at time t^{n+1} by following the characteristics.

- Step 3: Deposition of particles localized at $(x^\star_k, y^\star_l)$

$$f^{n+1}_{i,j} = \left(\sum_{k,l} w^n_{k,l} S(x_i - x^\star_k) S(y_j - y^\star_l)\right) / (J_s B^*_{||s})_{i,j}$$

3.3 Numerical experiments

3.3.1 Accuracy of conservation of invariants

An equilibrium solution of the collisionless gyrokinetic equation must satisfy some conditions. To get an equilibrium for the Vlasov equation, it suffices to take an arbitrary function of constants of motion in the unperturbed characteristics. In an axisymmetric toroidal configuration, a gyrokinetic Vlasov equilibrium is defined by three constants of motion: the magnetic moment μ, the energy $\mathcal{E}=v_\parallel^2/2+\mu\, B(r,\theta)$, and the canonical toroidal angular momentum [AGG+11] $P_\varphi=\psi(r)+I v_\parallel/B(r,\theta)$. The $\psi(r)$ function is defined thanks to the safety factor $q(r)$ by the relation: $d\psi/dr=-B_0\, r/q(r)$.

To get a good accuracy in integrating the Vlasov equation in time, and then to conserve exactly an initial equilibrium distribution function, we have to take care of the correctness of:

- the initial equilibrium setting; distribution function will be a function of the constants of motion: $\mu, \mathcal{E}, P_\varphi$;
- computing the displacements in the Vlasov solver (finding the foot of the characteristic); a sufficiently small time step has to be chosen for the time integration scheme for example, but also the resolution in space must be sufficient to have enough accuracy to interpolate displacement fields;
- interpolate the distribution function in the Vlasov solver with enough resolution; the number of points in the computational domain has to be tuned for this issue;

We will be able to estimate quantitatively the quality of the distribution function after several time steps by:

- measuring the difference between the initial equilibrium function and the distribution function at a given time step.

3.3.2 First test case: equilibrium conservation

The initial distribution function is set up to

$$f_{t=0}(r,\theta,\varphi,v_\parallel) = \mathbf{1}_{[P_{\varphi 1},P_{\varphi 2}]}(P_\varphi - P_{\varphi 1})^m (P_\varphi - P_{\varphi 2})^m \, sin(\gamma\, P_\varphi) \tag{18}$$

where the invariant P_φ is a function of $r, \theta, v_\parallel$ and $\mathbf{1}$ is the indicator function. We will look at

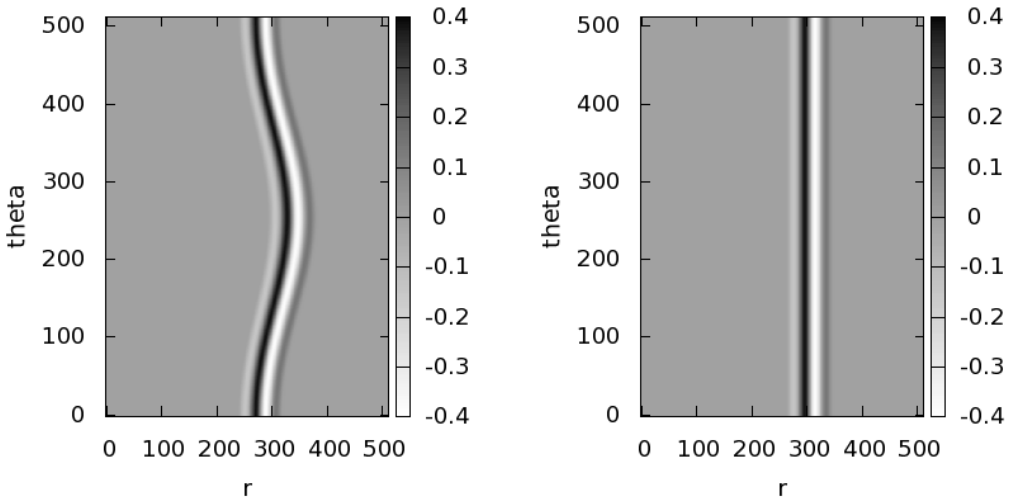

Figure 1: Initial function $f_{t=0}$ at $v_\parallel=-3\, v_{th0}, \varphi=0$ (left), $v_\parallel=0, \varphi=0$ (right)

the norms $u_p(t) = \|f_t - f_{t=0}\|_p$ with $p = 1, \infty$. They are defined as

$$u_\infty(t) = sup\{|f_t - f_{t=0}| : \forall (r,\theta,\varphi,v_\parallel)\}$$
$$u_1(t) = \int |f_t - f_{t=0}| J_s B^*_{||s} dr d\theta d\varphi dv_\parallel$$

Let us take the following parameters : $\gamma = 4\pi/(P_{\varphi 2} - P_{\varphi 1})$, $m = 1$, $\rho^* = 0.01$. The values $(P_{\varphi 1}, P_{\varphi 2})$ are choosen adequately in order to have an interval $[P_{\varphi 1}, P_{\varphi 2}]$ that is strictly included

in the computational domain $r \in [r_{min}, r_{max}], \theta \in [0, 2\pi], v_{\|} = -3\, v_{th0}$. A poloidal cut of this initial function is sketched for two values of parallel velocity in Figure 1. As the initial function depends only on the invariant P_φ, it should be conserved by time integration of the Vlasov equation. The duration of the experiment is denoted t_{max}. The timing unit is the ion cyclotronic time Ω^{-1}, it will also be the case in all plots of this document. The Vlasov equation is solved during all time steps with Φ forced to zero. An ideal simulation should preserve all norms $\forall p,\ \ u_p(t) = 0$. Practically and in the worst case, the function $u_p(t)$ will move quickly away from 0 as t grows.

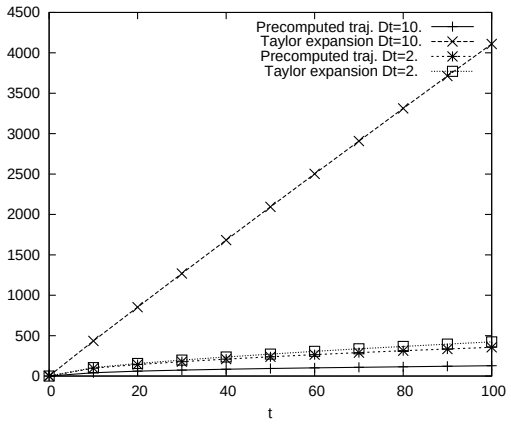

Figure 2: Evolution of the L_1 norm $u_1(t)$ with $N_r = 512, N_\theta = 512$

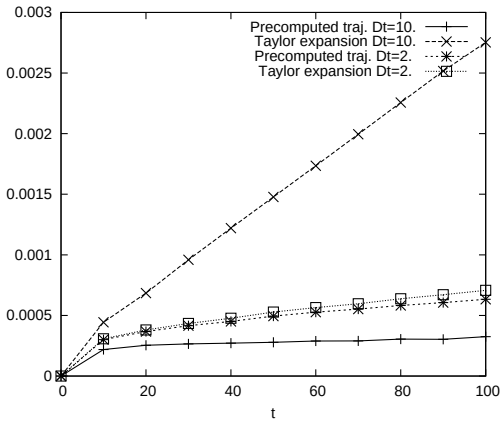

Figure 3: Evolution of the L_∞ norm $u_\infty(t)$ with $N_r = 512, N_\theta = 512$

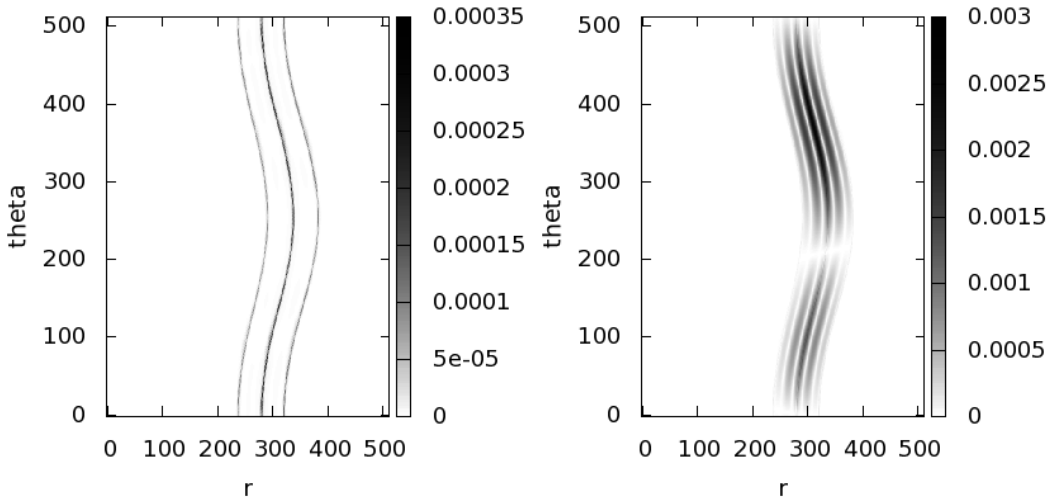

Figure 4: distance between f_t and $f_{t=0}$ (modulus of the difference) at $t = 100$ with $\Delta t = 10$ and *Precomputed trajectories* (left), distance $\|f_t - f_{t=0}\|$ at $t = 100$ with $\Delta t = 10$ and *Taylor expansion* (right)

In the experiment of Figures 2 and 3, the L_1, L_∞ norms are drawn for some simulations. A comparison is made between the two methods presented previously that are used to calculate the feet of the characteristics. The parameter Δt is set to 2 and 10, which is near typical values used in GYSELA simulations and $t_{max} = 100$. The computational domain is quite refined in (r, θ) with $N_r = 512, N_\theta = 512$. One can remark that *Precomputed trajectories* strategy is more accurate than *Taylor expansion*. Nevertheless, the difference shown here is significant for $\Delta t = 10$, but quite negligible for small $\Delta t = 2$. On Figure 4, the differences to the initial distribution function at final state, are shown for an arbitrary value of $v_{\|} = -3\, v_{th0}$. One can see here where errors are located using both strategies: *Precomputed trajectories* at the center, and *Taylor expansion* at right. One can see that the amplitude of the error is larger in the case of *Taylor Expansion*, and also less spatially localized.

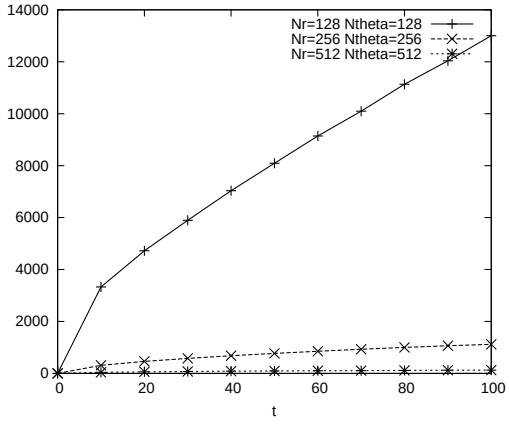

Figure 5: Evolution of the L_1 norm $u_1(t)$ for different poloidal mesh sizes

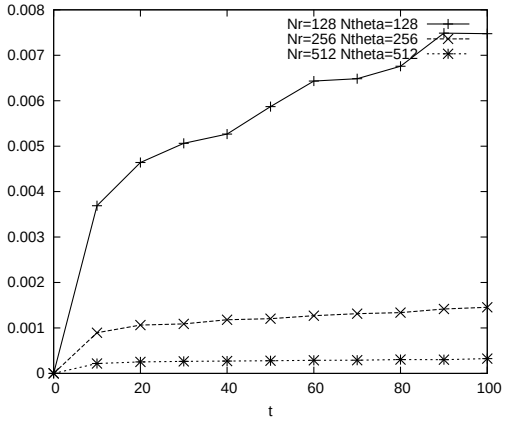

Figure 6: Evolution of the L_∞ norm $u_\infty(t)$ for different poloidal mesh sizes

On Figures 5 and 6, some L-p norms produced by three simulations are shown (*Precomputed trajectories* method is used). Between two consecutive simulations, the sizes of the domain (N_r, N_θ) have been multiplied by a factor two. While increasing (N_r, N_θ), one can notice that simulations become more and more accurate, *i.e.* L-p norms are reduced. The increase rate of the error depends on the factor $N_r\, N_\theta$.

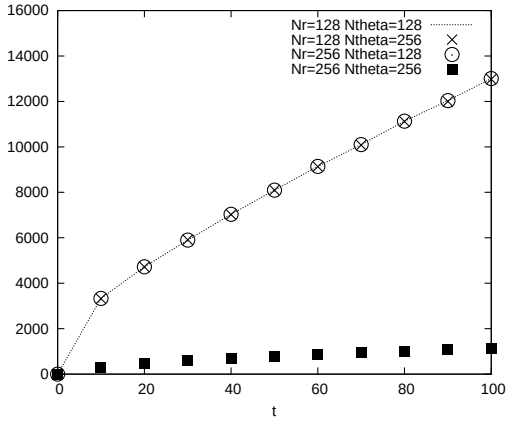

Figure 7: Evolution of the L_1 norm $u_1(t)$ for different poloidal mesh sizes

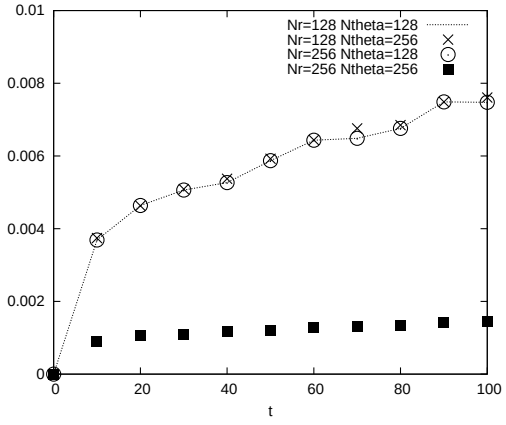

Figure 8: Evolution of the L_∞ norm $u_\infty(t)$ for different poloidal mesh sizes

The domain sizes N_r and N_θ are increased independantly each other in the Figures 7 and 8 (*Precomputed trajectories* method is used). It is clear that the error is only of the order of the smallest size among N_r and N_θ sizes. As far as Equations (11,12) are concerned, it is then noteworthy that N_r and N_θ should be chosen close to each other in order to improve accuracy.

3.3.3 Second test case: shear flows

Compared to the previous experiments, the initial distribution function considered in the present section is taken with an inhomogeneity in θ. Only the *Precomputed trajectories* method has been used for these simulations, because it is more accurate in any case. As variable θ is not an invariant, the distribution function is expected to evolve in time. For the sake of simplicity and to reduce computational costs, the simulation is setup with $N_\varphi = 1, N_{v_\parallel} = 1$. The initial distribution function is now

$$f_{t=0}(r,\theta,\varphi,v_\parallel) = \mathbf{1}_{[P_{\varphi 1},P_{\varphi 2}]}(P_\varphi - P_{\varphi 1})^m (P_\varphi - P_{\varphi 2})^m \mathbf{1}_{[\theta_1,\theta_2]}(\theta-\theta_1)^m(\theta-\theta_2)^m$$

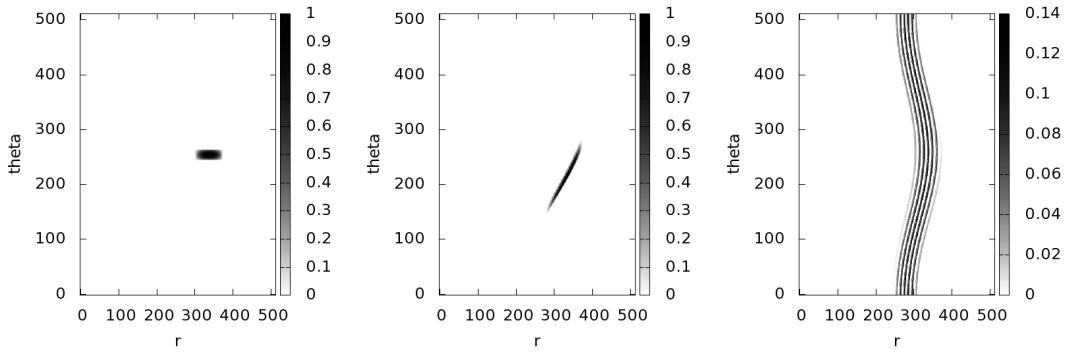

Figure 9: Initial function $f_{t=0}$ with $v_\parallel = -3\, v_{th0}$, $N_r = 512$, $N_\theta = 512$ (left), distribution function f at $t = 2000$ with BSL scheme (middle), distribution function f at $t = 50000$ with BSL scheme (right)

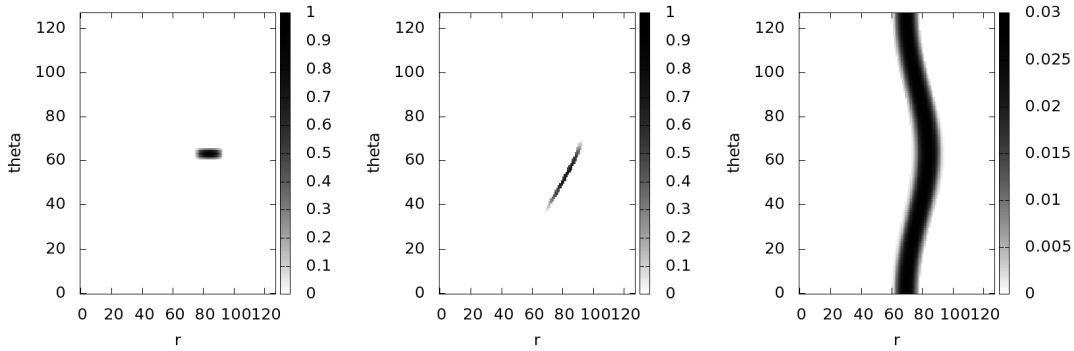

Figure 10: Initial function $f_{t=0}$ with $v_\parallel = -3\, v_{th0}$, $N_r = 128$, $N_\theta = 128$ (left), distribution function f at $t = 2000$ with BSL scheme (middle), distribution function f with BSL scheme at $t = 50000$ (right)

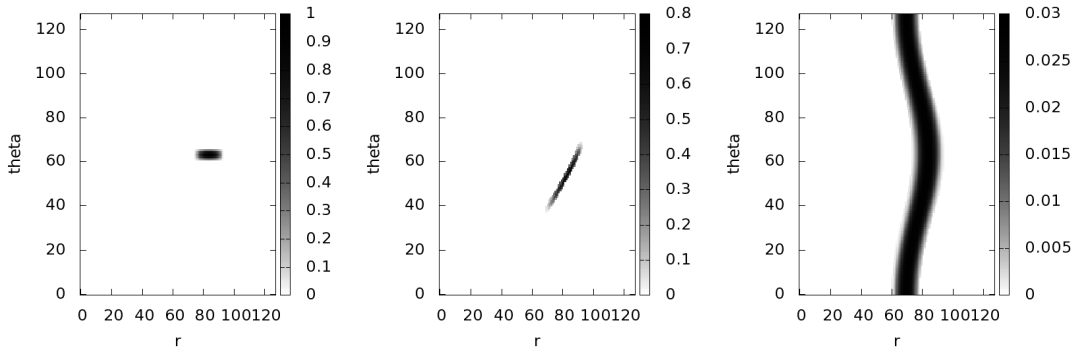

Figure 11: Initial function $f_{t=0}$ with $v_\parallel = -3\, v_{th0}$, $N_r = 128$, $N_\theta = 128$ (left), distribution function f at $t = 2000$ with FSL scheme (middle), distribution function f at $t = 50000$ with FSL scheme (right)

On Figures 9, 10, 11, the distribution function is shown for different time steps (parallel velocity is $v_\parallel = -3\, v_{th0}$, m is set to 1, , $\rho^* = .01$). One can notice the shearing that appears along time. The system dynamics tends to create filamentation in configuration space. Nevertheless, the mass $\|f\|_1 = \int f\, J_s\, B^\star_\parallel dr d\theta d\phi dv_\parallel$ and the maximum value $\|f\|_\infty = sup\{|f| : \forall (r, \theta, \phi, v_\parallel)\}$ should theoretically be conserved at any time. Finer structures than mesh element size are dynamically created (see the rightmost plot of Figure 9), and they can not be correctly captured (filamentation induces that mass can be lost or gained at each time step). As it can be seen in Figures 12 and 13, with the classical Backward Semi-Lagrangian scheme $\|f\|_\infty$ quantity does not remain constant, $\|f\|_1$ is well conserved at $(N_r = 512, N_\theta = 512)$ while $(N_r = 128, N_\theta = 128)$ does not lead to good conservation of $\|f\|_1$. It is noteworthy, that finer resolution in space - going from $(N_r = 128, N_\theta = 128)$ to $(N_r = 512, N_\theta = 512)$ greatly improves the conservation of mass and of the largest absolute value. If one takes the Forward Semi-Lagrangian scheme, the Figures 12 and 13 illustrate that $\|f\|_\infty$ behaves like BSL but $\|f\|_1$ is better preserved, as expected. Then, FSL scheme is a good solution as far as mass conservation is required.

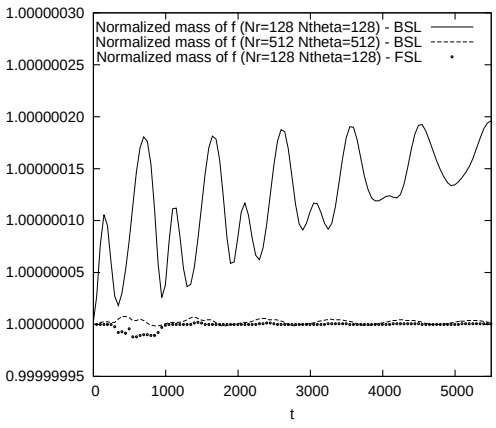

Figure 12: Time evolution of the mass of f for different poloidal mesh sizes

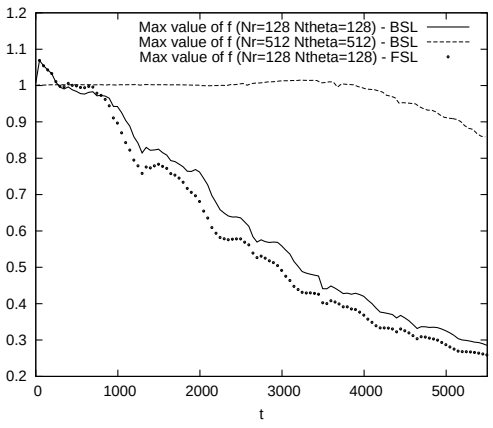

Figure 13: Evolution of the f maximum value for different poloidal mesh sizes

Let suppose one wants to keep the framework of the Backward Semi-Lagrangian scheme and to avoid FSL, another solution to preserve mass could be to have an aligned mesh. If one change the variables $(r, \theta, \varphi, v_\parallel)$ to $(P_\varphi, \theta, \varphi, v_\parallel)$, the two initial distribution functions we have seen are more accurately discretized. Also, the conservation of mass is improved for the following reason: advection is done only in the direction θ, there is no shift along the P_φ direction. The displacement in the poloidal plane during one time step amounts to shift only in θ. So mass has just to be conserved on each mesh line labelled by P_φ, and it will automatically give global mass conservation. It is easy to construct an advection operator and the associated interpolation scheme that preserve mass on each mesh line P_φ. Another benefit is that in this new set of variables, the equilibrium function is better discretized and represented: steep gradient is only in P_φ direction in the poloidal plane. Nevertheless, building and managing a mesh that includes P_φ variable is much more difficult to implement.

3.3.4 Extrapolation to nonlinear test cases

The first test case of section 3.3.2 is linked to what is going on at the beginning of a Gysela run. The initial distribution function is a perturbed equilibrium. One wishes to remain close to this quasi-equilibrium (if the amplitude of electric potential is very small) without beeing too much biased by some large numerical artifacts of the linear operator that we have seen: artificial increase of u_1, u_∞.

The second test case of section 3.3.3 is near what is happening in non-linear dynamics in which many localized spatial structures develop and grow. One expect to conserve the total particle density, even if the distribution function becomes something else than an ideal function of motion invariants. The decrease of maximal value of Figure 13 is not acceptable to perform accurate simulations. Aligned coordinates along P_φ should be able to improve conservation of $\|f\|_\infty$.

4 Nonlinear gyrokinetic simulations

4.1 Split linear and nonlinear parts

4.1.1 Global separation of linear/nonlinear terms

The equations (1,2) can be split into two parts (in the same spirit that [IIK$^+$08]). The first part includes the nonlinear terms that depends on the electric potential. The second part comprises the other terms. One can solve these two parts one after the other by splitting. On the first hand, the linear operator is presented in Eqs (19,20), on the second hand, the nonlinear operator is described by Eqs (21,22).

Linear operator $\mathcal{L}$

$$\frac{\mathrm{d}x^i}{\mathrm{dt}} = v_\parallel \vec{b}^*_s \cdot \vec{\nabla} x^i + \vec{v}_{Ds} \cdot \vec{\nabla} x^i \quad (19)$$

$$m_s \frac{\mathrm{d}v_\parallel}{\mathrm{dt}} = -\mu \vec{b}^*_s \cdot \vec{\nabla} B \quad (20)$$

Nonlinear operator $\mathcal{N}$

$$\frac{\mathrm{d}x^i}{\mathrm{dt}} = \vec{v}_{Es_{GC}} \cdot \vec{\nabla} x^i \quad (21)$$

$$m_s \frac{\mathrm{d}v_\parallel}{\mathrm{dt}} = -e_s \vec{b}^*_s \cdot \vec{\nabla} \bar{\phi} + \frac{m_s v_\parallel}{B} \vec{v}_{Es_{GC}} \cdot \vec{\nabla} B \quad (22)$$

The linear operator exhibits large displacements at large modulus of parallel velocity, and also induces shear flows. These features can interfere with the nonlinear dynamics that eventually involves small displacements that are not of the same order of magnitude. Moreover, as the dynamics generated by the two operators are different, induced accuracy problems have possibly not the same characteristics for the two operators; and the limitations (CFL-like conditions) on the time step are also not the same. Ideally, one should be able to fix the time step of linear and nonlinear operators independantly in order to enhance accuracy.

The original formulation that uses Strang splitting in phase space for the Vlasov solver, but without a linear/nonlinear splitting, can leed to serious troubles at high parallel velocities. Indeed, directional splitting suffers from some large shifts in φ, r and θ at each directional advection (section 3.2). Then, for not so large Δt, the evaluation of electric fields $E_{(.)}$ is not done at the right spatial position at each substep of the splitting except for the first substep of the splitting. One has to take very small time step to recover small displacements in the linear operator and then a reasonable accuracy in the evaluation of $E_{(.)}$.
The splitting between linear and nonlinear parts eliminates this problem. The nonlinear operator is applied alone, thus the linear operator and its large shifts does not interact badly with nonlinear solver. The proposed solution is to perform at each time step: first, a directional splitting for the linear operator $\mathcal{L}$ with the sequence $(\hat{v_\parallel}/2, \hat{\varphi}/2, \hat{r\theta}, \hat{\varphi}/2, \hat{v_\parallel}/2)$, second, a directional splitting for the nonlinear operator $\mathcal{N}$ with the same sequence $(\hat{v_\parallel}/2, \hat{\varphi}/2, \hat{r\theta}, \hat{\varphi}/2, \hat{v_\parallel}/2)$.

This approach is a liitle bit expensive in term of computational cost because it nearly doubles time to solution.

4.1.2 Conservation of mass

Each of the operators $\mathcal{L}, \mathcal{N}$ conserves the mass independently. One can track during simulation which operator degrades or not the total mass.

4.2 Experiments

In the following GYSELA runs, the BSL and FSL schemes are compared for two test cases with μ =0 (4D only). Results for both BSL scheme and FSL scheme are shown. In the FSL version that has been run, FSL scheme is present in all advections: 1D $(\varphi, v_\parallel)$ and 2D (r, θ). The rest of the code is unchanged compared to the BSL version. In order to simplify boundary conditions in $v_\parallel$, the distribution function is fixed at v_{min} and v_{max}. Therefore, we have also taken this choice for the BSL runs presented hereafter.

4.2.1 Cylindrical case

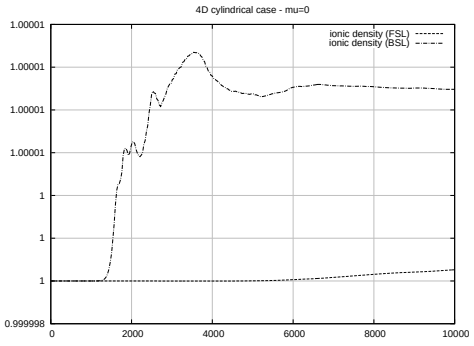

Figure 14: Evolution of the mass for a 4D, $\mu = 0$, cylindrical test case

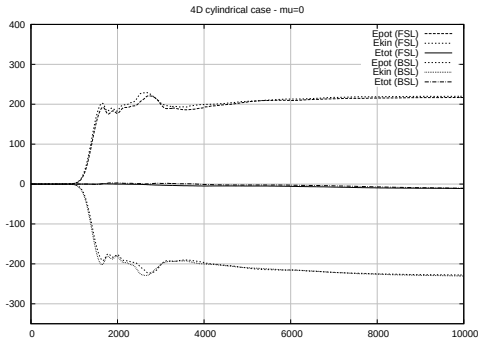

Figure 15: Evolution of the energies for a 4D, $\mu = 0$, cylindrical test case

Some plots for our reference test case `data4D_slab_A32` ($\rho^* = 1/32$, $\mu = 0$) is given in Fig. (14,15,21,22). The computational domain size is $N_r = 128, N_\theta = 256, N_\varphi = 32, N_{v_\parallel} = 48$.

The mass is well preserved with FSL as it can be seen on Fig. 14. Potential energy, kinetic energy and total energy are presented on Fig.15. The total energy should theoretically remains at zero, the two schemes are quite proximate to that. During the beginning of the simulation, FSL and BSL give quite similar electric potential as it is shown at time $t = 1920$ in Fig. (21,22). Nevertheless, after a while, the two schemes diverges slowly (see for example $t = 8000$).

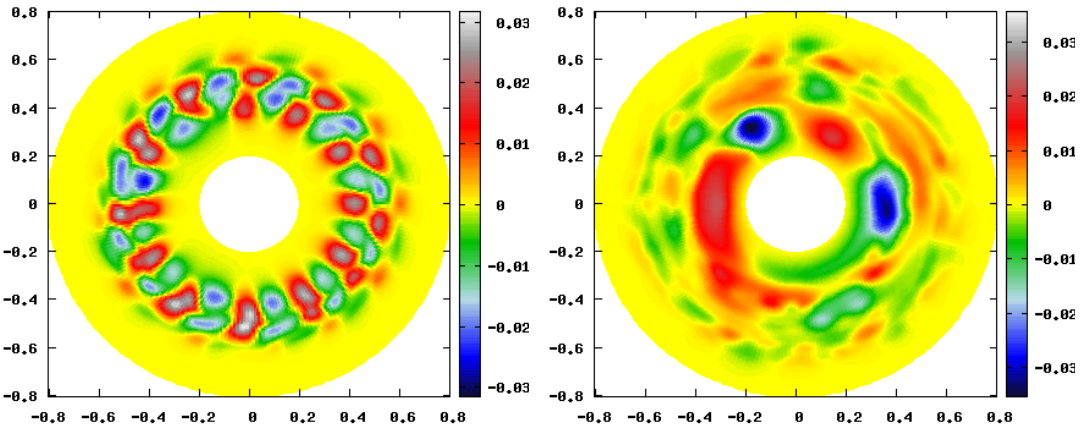

Figure 16: Poloidal cut of electric potential at different time steps ($t = 1920$ left, $t = 8000$ right), $\varphi = 0$, **BSL** scheme

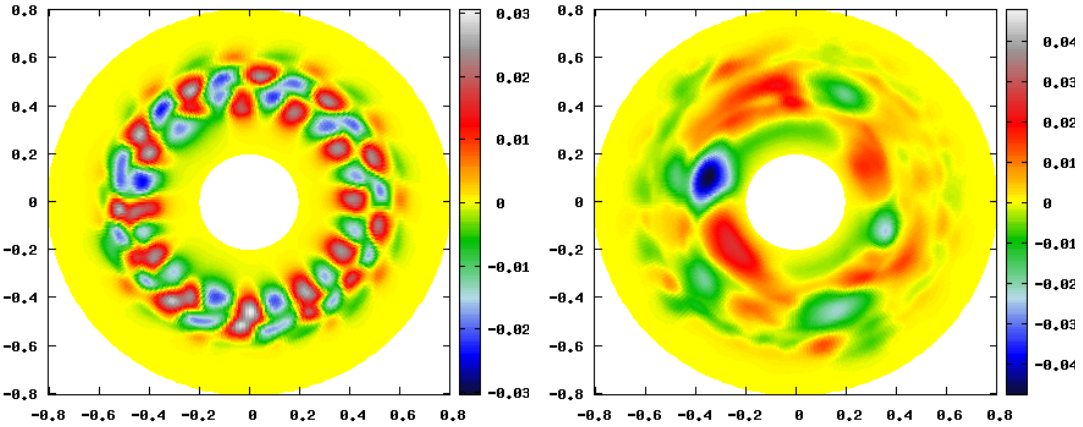

Figure 17: Poloidal cut of electric potential at different time steps ($t = 1920$ left, $t = 8000$ right), $\varphi = 0$, **FSL** scheme

4.2.2 Toroidal case

A small toroidal test case has been set up ($\rho^* = 1/40$). The computational domain size is $N_r = 256, N_\theta = 256, N_\varphi = 64, N_{v_\parallel} = 48$. The FSL version outperforms the BSL version from the point of view of mass conservation. The conservation of total energy is far more better with FSL and this is due to improved mass conservation. A precise tracking of mass losses/gains allows us to conclude that the linear operator $\mathcal{L}$ is mainly responsible for mass degradation using BSL approach. An explanation is that in toroidal setting, $\mathcal{L}$ causes large displacements, whereas in cylindrical setting (previous subsection) this was not the case.

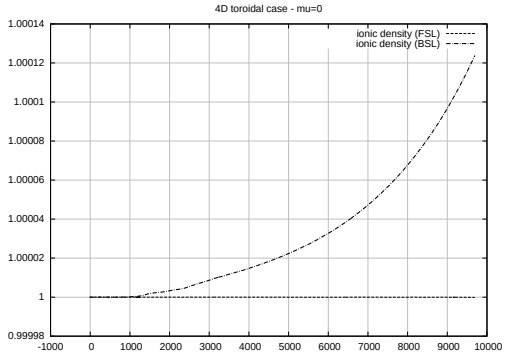

Figure 18: Evolution of the mass for a 4D, $\mu = 0$, toroidal test case

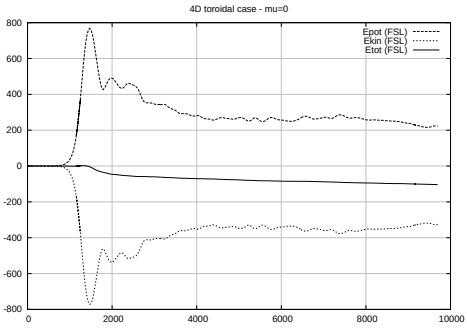

Figure 19: Evolution of the energies for a 4D, $\mu = 0$, toroidal test case with FSL

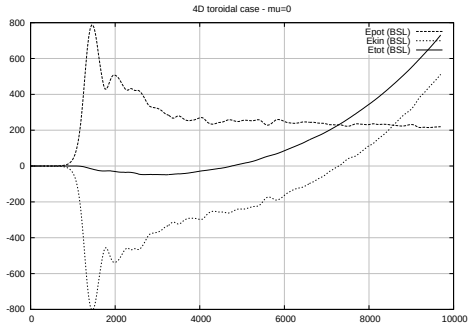

Figure 20: Evolution of the energies for a 4D, $\mu = 0$, toroidal test case with BSL

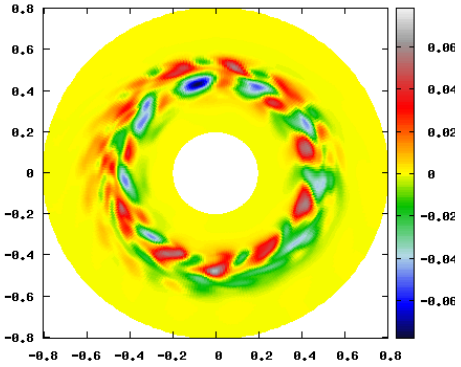

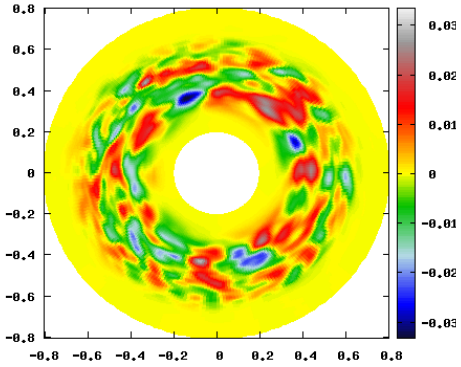

Figure 21: Poloidal cut of electric potential at different time steps ($t = 1600$ left, $t = 4800$ right), $\varphi = 0$, **BSL** scheme

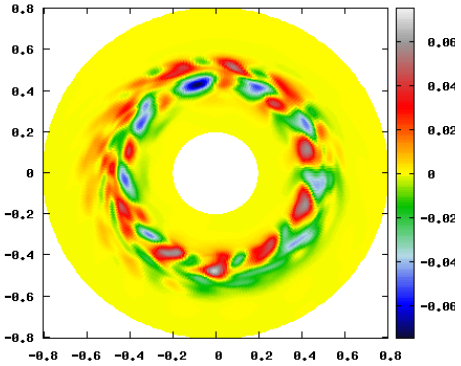

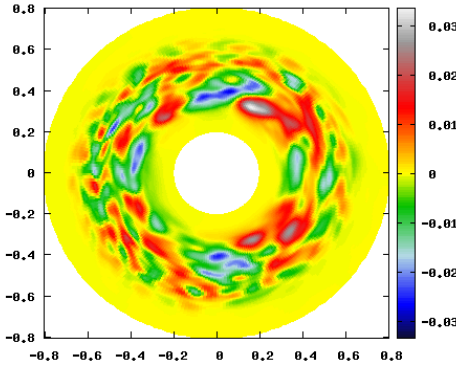

Figure 22: Poloidal cut of electric potential at different time steps ($t = 1600$ left, $t = 4800$ right), $\varphi = 0$, **FSL** scheme

5 Conclusion

Few solutions have been proposed to help preserving constant states, L_1 and $_\infty$ norms in gyrokinetic semi-Lagrangian simulations. Some GYSELA runs show that we get benefits from these improvements in term of accuracy.

References

[ABH+06] P. Angelino, A. Bottino, R. Hatzky, S. Jolliet, O. Sauter, T. M. Tran, and L. Villard. On the definition of a kinetic equilibrium in global gyrokinetic simulations. *Physics of Plasma*, 13(5):052304, 2006.

[AGG+11] J. Abiteboul, X. Garbet, V. Grandgirard, S. J. Allfrey, Ph. Ghendrih, G. Latu, Y. Sarazin, and A. Strugarek. Conservation equations and calculation of mean flows in gyrokinetics. *Physics of Plasmas*, 18(8):082503, 2011.

[BCG+11] Jean-Philippe Braeunig, Nicolas Crouseilles, Virginie Grandgirard, Guillaume Latu, Michel Mehrenberger, and Eric Sonnendrücker. Some numerical aspects of the conservative PSM scheme in a 4D drift-kinetic code. Technical report, INRIA, December 2011. http://hal.archives-ouvertes.fr/hal-00650343.

[CRS09] Nicolas Crouseilles, Thomas Respaud, and Eric Sonnendrücker. A forward semi-lagrangian method for the numerical solution of the vlasov equation. *Computer Physics Communications*, 180(10):1730–1745, 2009.

[GBB+06] V. Grandgirard, M. Brunetti, P. Bertrand, N. Besse, X. Garbet, P. Ghendrih, G. Manfredi, Y. Sarazin, O. Sauter, E. Sonnendrucker, J. Vaclavik, and L. Villard. A drift-kinetic Semi-Lagrangian 4D code for ion turbulence simulation. *Journal of Computational Physics*, 217(2):395 – 423, 2006.

[GSG+08] V. Grandgirard, Y. Sarazin, X. Garbet, G. Dif-Pradalier, Ph. Ghendrih, N. Crouseilles, G. Latu, E. Sonnendrucker, N. Besse, and P. Bertrand. Computing ITG turbulence with a full-f semi-Lagrangian code. *Communications in Nonlinear Science and Numerical Simulation*, 13(1):81 – 87, 2008.

[Hah88] T. S. Hahm. Nonlinear gyrokinetic equations for tokamak microturbulence. *Physics of Fluids*, 31(9):2670–2673, 1988.

[IIK+08] Yasuhiro Idomura, Masato Ida, Takuma Kano, Nobuyuki Aiba, and Shinji Tokuda. Conservative global gyrokinetic toroidal full-f five-dimensional vlasov simulation. *Computer Physics Communications*, 179(6):391 – 403, 2008.

[SGA+11] Y. Sarazin, V. Grandgirard, J. Abiteboul, S. Allfrey, X. Garbet, Ph. Ghendrih, G. Latu, A. Strugarek, G. Dif-Pradalier, P.H. Diamond, S. Ku, C.S. Chang, B.F. McMillan, T.M. Tran, L. Villard, S. Jolliet, A. Bottino, and P. Angelino. Predictions on heat transport and plasma rotation from global gyrokinetic simulations. *Nuclear Fusion*, 51(10):103023, 2011.

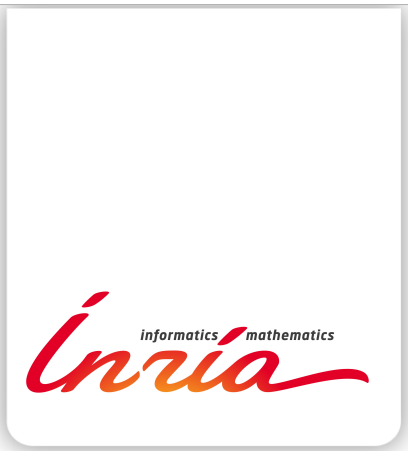

RESEARCH CENTRE
NANCY – GRAND EST

615 rue du Jardin Botanique
CS20101
54603 Villers-lès-Nancy Cedex

Publisher
Inria
Domaine de Voluceau - Rocquencourt
BP 105 - 78153 Le Chesnay Cedex
inria.fr

ISSN 0249-6399